







Ultra-delayed Neutrino-driven Explosion of Rotating Massive-star Collapse

Sho Fujibayashi¹ , Koh Takahashi¹ , Yuichiro Sekiguchi^{2,3} , and Masaru Shibata^{1,2} 

¹ Max-Planck-Institut für Gravitationsphysik (Albert-Einstein-Institut), Am Mühlenberg 1, D-14476 Potsdam-Golm, Germany; sho.fujibayashi@aei.mpg.de

² Center for Gravitational Physics, Yukawa Institute for Theoretical Physics, Kyoto University, Kyoto, 606-8502, Japan

³ Department of Physics, Toho University, Funabashi, Chiba 274-8510, Japan

Received 2021 February 8; revised 2021 June 7; accepted 2021 June 10; published 2021 September 28

Abstract

Long-term neutrino-radiation hydrodynamics simulations in full general relativity are performed for the collapse of rotating massive stars that are evolved from He-stars with initial masses of 20 and 32 M_{\odot} . It is shown that if the collapsing stellar core has sufficient angular momentum, the rotationally supported proto-neutron star (PNS) survives for seconds accompanying the formation of a massive torus of mass larger than 1 M_{\odot} . Subsequent mass accretion onto the central region produces a massive and compact central object, and eventually enhances the neutrino luminosity beyond 10^{53} erg s⁻¹, resulting in a very delayed neutrino-driven explosion, in particular toward the polar direction. The kinetic energy of the explosion can be appreciably higher than 10^{52} erg for a massive progenitor star and compatible with that of energetic supernovae like broad-line type-Ic supernovae. By the subsequent accretion, the massive PNS collapses eventually into a rapidly spinning black hole, which could be a central engine for gamma-ray bursts if a massive torus surrounds it.

Unified Astronomy Thesaurus concepts: Core-collapse supernovae (304); Type Ic supernovae (1730)

Supporting material: animations

1. Introduction

Core-collapse supernovae (SNe) are explosive events that occur at the final stage of massive-star evolution. In the typical scenario (e.g., Janka et al. 2012), after the collapse of the iron core of the progenitor star, a proto-neutron star (PNS) is first formed. Then, a shock wave is generated at the inner core of the PNS and propagates outward sweeping up matter. However, because of the photodissociation of iron, the shock stalls in the middle of the propagation. Subsequently, heating by neutrinos emitted from the PNS is believed to play a key role for supplying energy to the stalled shock (Bethe & Wilson 1985). If the neutrino-heating timescale becomes shorter than that of matter infall from the outer envelop, the stalled shock is revived and the explosion is driven by neutrino heating (Janka 2001). In contrast, if the neutrino heating is not efficient enough, the stalled shock eventually goes back to the PNS and a black hole (BH) is formed. In particular, for high-mass progenitor stars with a zero-age main-sequence (ZAMS) mass of $M_{\text{ZAMS}} \gtrsim 40 M_{\odot}$ (Woosley et al. 2002), the naive expectation for the final fate is the formation of a BH without shock revival.

As summarized above, the key quantity for a successful explosion is the efficiency of the neutrino heating (Janka 2001). In fact, many sophisticated simulations of core-collapse SNe have shown that the success of the SN explosion depends sensitively on the neutrino luminosity and neutrino-heating efficiency (for the latest numerical simulations in this field, see, e.g., Müller et al. 2012; Burrows et al. 2019; Nakamura et al. 2019; Bollig et al. 2021; Kuroda et al. 2020; Mezzacappa et al. 2020; Müller 2020; Stockinger et al. 2020; Harada et al. 2020; Obergaulinger & Aloy 2020).

In this paper, we propose a mechanism by which the neutrino luminosity of the central object is naturally enhanced for very high-mass rotating progenitor stars. We consider a rotating progenitor core, which results in a PNS rapidly rotating with a rotational period of ≤ 1 ms and is surrounded by a massive torus with a mass higher than 1 M_{\odot} . Due to rapid rotation, a PNS with a

rest mass $\gtrsim 3 M_{\odot}$ can survive with an equation of state (EOS) with which the maximum gravitational mass for cold non-rotating neutron stars (NSs), M_{max} , is larger than 2 M_{\odot} . This appreciably increases the lifetime of the PNS. In addition, due to the presence of a compact massive torus as well as the high mass of the PNS, the total neutrino luminosity is enhanced during the evolution of the system. Furthermore, because of the flattened geometry of these central objects, the neutrino flux is enhanced in the polar region. As a consequence, the neutrino heating timescale of the stalled shock becomes shorter than the timescale of the matter infall in the polar region, leading to a bipolar explosion.

By performing numerical-relativity simulations, we will illustrate that this mechanism can indeed work for a rapidly rotating progenitor of $M_{\text{ZAMS}} \approx 45\text{--}65 M_{\odot}$, which corresponds to a range of He-core masses of $M_{\text{He}} = 20\text{--}32 M_{\odot}$. For such high-mass rapidly rotating progenitors, the total mass of the PNS and surrounding torus becomes also high, and hence, the neutrino luminosity is enhanced as well. As a result, the bipolar outflow becomes more energetic than for ordinary SNe. Thus, this mechanism may produce a class of energetic SNe like broad-line type-Ic SNe (see, e.g., Woosley & Bloom 2006; Cano et al. 2017 for reviews).

This article is organized as follows. In Section 2, we summarize the progenitor models employed as the initial conditions for the numerical-relativity simulations together with a brief summary of our method for the simulations. The results for the successful explosions are shown in Section 3. Section 4 is devoted to a summary and discussion.

2. Models and Method

We employ the final state of high-mass stellar-evolution models as the initial conditions of our numerical-relativity simulations. The stellar evolutions of non-rotating He-star models with initial mass of $M_{\text{He}} = 20$ and 32 M_{\odot} are calculated using the code described in Takahashi et al. (2018). For these models, $M_{\text{ZAMS}} \approx 45$ and 65 M_{\odot} , respectively (Woosley et al. 2002).

Table 1
List of the Models and the Results

Model	M_{He} (M_{\odot})	Ω_0 (rad s^{-1})	R_0 (km)	$(\chi_{5M_{\odot}}, \chi_{10M_{\odot}})$	t_{exp} (s)	t_{BH} (s)	E_{exp} (10^{51} erg)
M20-0	20	0	...	(0, 0)	...	0.3	...
M20-S040	20	0.40	6000	(1.0, 0.34)	...	1.1	...
M20-S050	20	0.50	6000	(1.3, 0.43)	3.3	4.3	4.2
M20-S075	20	0.75	6000	(1.9, 0.65)	4.8	7.2	4.5
M20-S100	20	1.00	6000	(2.5, 0.87)	5.9	9.8	3.6
M20-L050	20	0.50	8500	(2.2, 1.1)	7.4	9.1	1.2
M20-S050N	20	0.50	6000	(1.3, 0.43)	3.5	4.3	1.7
M32-0	32	0	...	(0, 0)	...	0.1	...
M32-S050	32	0.50	5800	(1.1, 0.61)	...	1.0	...
M32-S075	32	0.75	5800	(1.7, 0.92)	2.7	4.3	52
M32-S100	32	1.00	5800	(2.3, 1.2)	3.2	5.1	26
M32-S075DD2	32	0.75	5800	(1.7, 0.92)	2.8	4.4	58
M32-S075N	32	0.75	5800	(1.7, 0.92)	3.0	4.3	11
M32-S075-modE	32	0.75	5800	(1.7, 0.92)	2.6	4.3	66

Note. t_{exp} and t_{BH} denote the post-bounce time at the onset of the explosion and that of BH formation, respectively.

The evolution calculations are performed until the central temperature reaches $\approx 8 \times 10^9$ K. At this stage, the central density is $\approx 8 \times 10^8 \text{ g cm}^{-3}$ for $M_{\text{He}} = 20 M_{\odot}$ and $\approx 5 \times 10^8 \text{ g cm}^{-3}$ for $M_{\text{He}} = 32 M_{\odot}$.

Observationally, it is known that at least some broad-line type-Ic SNe are associated with gamma-ray bursts (GRBs; Cano et al. 2017), and theoretically, a broadly accepted candidate for the central engine of GRBs is a system composed of a rapidly spinning BH and a dense accretion torus. For the formation of the BH–torus system, a rapidly rotating progenitor star is obviously necessary (Woosley 1993; MacFadyen & Woosley 1999). Hence, we consider rapidly rotating massive stars as the progenitor of such energetic SNe. Rapidly rotating progenitors may be formed via peculiar single-star evolution (Yoon & Langer 2005; Woosley & Heger 2006) or by binary merger (e.g., Fryer & Heger 2005). Recent stellar-evolution simulations predict that the cores of the fastest rotating core-collapse progenitors may have $\approx 3 \times 10^{16} \text{ cm}^2 \text{ s}^{-1}$ of averaged specific angular momentum, or equivalently, ≈ 1.36 of the spin parameters, inside an enclosed mass of $5 M_{\odot}$ (Aguilera-Dena et al. 2018). These results should be interpreted with caution, however, as even the most advanced stellar-evolution simulations take into account the effects of angular-momentum transport via convection, circulation, and magnetohydrodynamics (MHD) in a phenomenological manner.

The other point to be stressed is that during the long-term evolution of the PNS and the torus surrounding it, which are the typical outcomes for rapidly rotating stellar core collapse, angular momentum transport can play an important role for the evolution of the system, because the timescale of viscous angular momentum transport, which is likely to stem from MHD instabilities, is typically several hundred milliseconds (Fujibayashi et al. 2018, 2020a, 2020b), while we follow the evolution of the system for seconds. It is also possible that MHD effects such as magnetic braking play an important role for angular momentum redistribution. Thus, the specific angular momentum distribution of the progenitor star is likely to be significantly modified during the long-term evolution of the system. However, currently, it is not clear how efficiently such angular momentum redistribution proceeds.

Thus in this paper, as a first step toward a more detailed study, we add a simple, ad-hoc angular momentum profile to

the final state of the evolved stars for the initial conditions, with which a system composed of a central object (either an NS or BH) surrounded by a massive torus is formed, even in the absence of angular momentum redistribution during the evolution of the collapse outcome (note that no angular momentum transport effect is taken into account in this work).

Specifically, the following cylindrical profile is imposed for the angular velocity:

$$\Omega = \Omega_0 e^{-R^2/R_0^2}, \quad (1)$$

where Ω_0 is the angular velocity along the rotation axis (z -axis), R is the cylindrical radius, and R_0 is the cut-off radius. This rotational profile is somewhat different from the one obtained in stellar-evolution simulations, in which the angular velocity is described as a function of the radius in spherical polar coordinates. However, because the contribution of matter along the rotation axis to the mass and angular momentum of the star is minor, the effects of the difference in the profile from spherically symmetric one is likely to be minor.

For R_0 , we choose the radius at the edge of the Si layer (L model), at which the entropy profile becomes discontinuous, or 70% of this radius (S model). Equation (1) implies that for $R \ll R_0$, the progenitor star is approximately rigidly rotating, while for the outer region, stellar matter rotates slowly. Such a state is reasonable if the efficiency of the angular momentum transport in the compact central region is sufficiently high. The steep cut-off of the angular velocity is achieved during the stellar evolution in the presence of the convective layer associated with the shell burning, in which the angular momentum at the bottom of the layer is transported to a large radius.

Table 1 lists the models considered in this work. M20 and M32 denote models with $M_{\text{He}} = 20$ and $32 M_{\odot}$, respectively. The letters ‘‘S’’ and ‘‘L’’ refer to the choice of R_0 and the following three-digit numbers denote the value of Ω_0 in units of 0.01 rad s^{-1} . We also perform simulations omitting neutrino pair-annihilation heating (models M32-S075N and M20-S050N) to show that this effect contributes substantially to increasing the explosion energy. To indicate the rapidness of the stellar rotation, in Table 1, we present a dimensionless spin

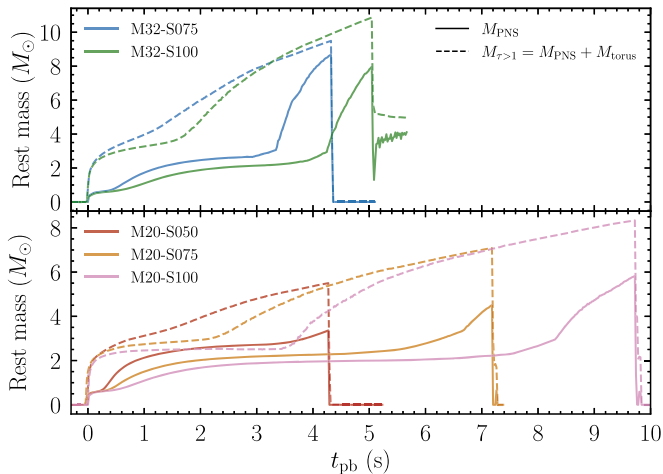


Figure 1. Evolution of the rest mass of the PNS (solid curves) and that in the optically thick region for neutrinos (dashed curves) for selected models. Note: by definition, the contribution from the torus is included in the value of M_{PNS} , and thus, it becomes very large just prior to the collapse to the BH. For the same reason, M_{PNS} has a finite value even after BH formation for model M32-S100.

parameter defined by $\chi_M = cJ/GM^2$, where J and M are, respectively, the total angular momentum and rest mass enclosed in mass shells at $M = 5 M_\odot$ and $10 M_\odot$. We note that the values of χ_M are broadly comparable to the results of a recent state-of-the-art stellar-evolution simulation (e.g., Aguilera-Dena et al. 2018).

A finite-temperature EOS referred to as SFHo (Steiner et al. 2013) is employed in this work except for model M32-S075DD2, in which another EOS referred to as DD2 (Banik et al. 2014) is employed for comparison. With the SFHo and DD2 EOSs, the maximum values of the gravitational mass for the non-rotating cold NSs are $M_{\text{max}} \approx 2.06$ and $2.42 M_\odot$, respectively, and the radii of the non-rotating NSs with a mass of $1.4 M_\odot$ are 11.9 and 13.2 km, respectively. The SFHo EOS is relatively soft in the sense that the value of M_{max} is close to $2 M_\odot$ and the radius is relatively small, $\lesssim 12$ km.

With the settings listed in Table 1, the PNS formed after the collapse is rapidly rotating and the resulting centrifugal force plays an important role to allow the rest mass of the PNS to exceed $3 M_\odot$ (see Figure 1 in Section 3). We note that several other simulations, for which we do not present the results in this article, already confirmed the collapse to a BH without shock revival for $\Omega_0 \leq 0.4 \text{ rad s}^{-1}$ for $M_{\text{He}} = 20 M_\odot$ and for $\Omega_0 \leq 0.5 \text{ rad s}^{-1}$ for $M_{\text{He}} = 32 M_\odot$. We also note that, for non-rotating models, the PNS collapses into a BH approximately at 0.1 s and 0.3 s after bounce for the $M_{\text{He}} = 32 M_\odot$ and $20 M_\odot$ models, respectively.

Numerical-relativity simulations are performed with our latest axisymmetric neutrino-radiation viscous hydrodynamics code. The details are described in Fujibayashi et al. (2017, 2020b). In this work, we do not take viscosity into account.

Einstein’s equation is solved with the original version of the puncture Baumgarte–Shapiro–Shibata–Nakamura formalism (Shibata & Nakamura 1995; Baumgarte & Shapiro 1999; Marronetti et al. 2008) incorporating the Z4c prescription (Hilditch et al. 2013) for constraint-violation propagation. We solve geometrical variables in Cartesian coordinates and employ the so-called cartoon method to impose axisymmetry to them (Shibata 2000; Alcubierre et al. 2001). The spatial interpolation

necessary for the cartoon process is carried out using accurate, fourth-order Lagrangian interpolation.

The radiation hydrodynamics equations are solved with a version of the leakage scheme together with a moment-transport scheme. The detailed description of the schemes is found in Sekiguchi (2010) and Fujibayashi et al. (2017). In this method, the emitted neutrinos are divided into “trapped” and “streaming” components. The trapped neutrinos are assumed to be thermalized with the fluid, and treated as a part of the fluid. In our numerical scheme, they are diffused out to the streaming component in the diffusion timescale.

The streaming neutrinos are solved using energy-integrated truncated-moment formalism (Shibata et al. 2011) with the so-called M1-closure relation to estimate the higher moments.⁴ Heating due to neutrino absorption and pair-annihilation is included in an approximate manner (Fujibayashi et al. 2017).

The free parameters of our leakage scheme (see Sekiguchi 2010 for the parameters) are phenomenologically determined. Specifically, we performed simulations for the collapse of a $15 M_\odot$ solar-metallicity progenitor (Woosley et al. 2002) and compared the neutrino luminosity at the core bounce with those found by Liebendörfer et al. (2003) and Janka et al. (2012). We then employ the parameters by which their neutrino luminosity curves are approximately reproduced. The heating of matter by streaming neutrinos is conservatively incorporated in this work: specifically, the heating term is reduced by a factor of $\exp(-2\tau_i)$ with the optical depth of i th species of neutrinos τ_i (i.e., this factor is multiplied to the opacity). Thus, only for sufficiently outside the neutrino spheres, is the heating efficient.

In energy-integrated neutrino-transfer schemes, the heating rate due to neutrino–matter interactions depends on the method for estimating the neutrino energy distribution through the energy dependence of the neutrino cross section (see, e.g., Foucart et al. 2016). To illustrate this dependence, we perform an additional simulation with the same setup as M32-S075, but with a different method for its estimation (see Appendix A for details and results).

For the numerical simulations, we employ the same nonuniform grid as that in our previous work (Fujibayashi et al. 2020b). In the inner region with $z < 15$ km and $R < 15$ km, the uniform grid is prepared with a grid spacing of 150 m. In the outer region, a nonuniform grid is prepared with an increased rate of grid spacing of 1.01. The computational domain is $0 \leq x \leq L$ and $0 \leq z \leq L$ with $L \approx 3 \times 10^4$ km.

3. Simulation Results

For all the simulations, a PNS is first formed after the stellar core collapse. Then, the baryon rest mass of the PNS increases

⁴ It is well-known that the crossing of multiple beams cannot be appropriately solved with moment-based schemes, and it can be a source of systematic errors on the neutrino distribution and heating rate in the system with a non-spherical hydrodynamical profile. In Sumiyoshi et al. (2021), the Eddington tensor was evaluated with a Boltzmann neutrino-transfer code and compared with that of the M1-closure relation for a system composed of a massive NS and a torus formed in a binary NS merger. It is found that the deviation of the Eddington tensor from that derived with the M1-closure is at most 10% in the edge of the NS and torus, and in the polar region the deviation is smaller. The system that we consider in this work has a similar profile to the one investigated by Sumiyoshi et al. (2021), and hence, we expect that the systematic errors associated with the moment-based scheme could not be significant, although for more quantitative studies a better radiation-transfer scheme, such as those used by Harada et al. (2020) and Foucart et al. (2020), is obviously required.

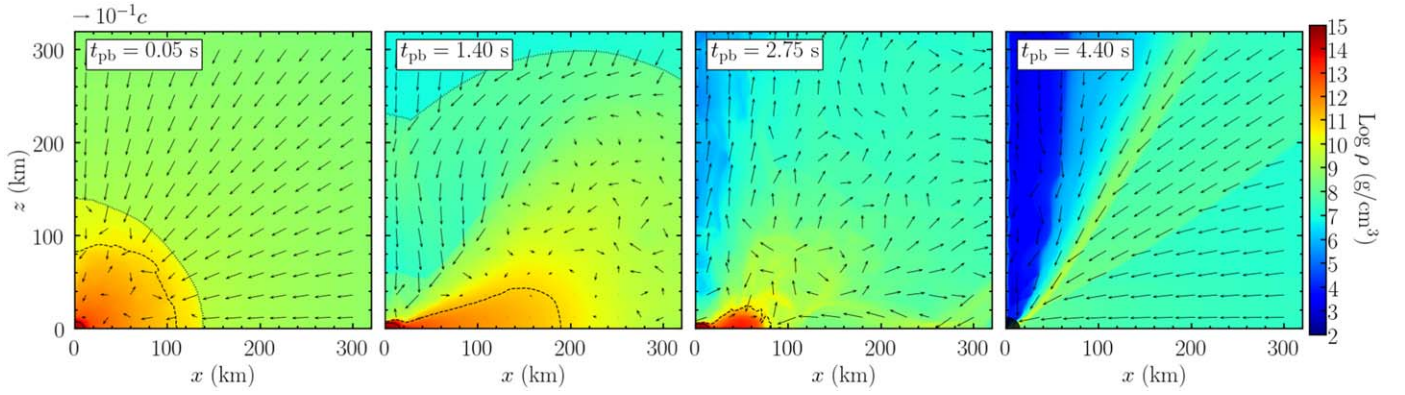


Figure 2. Snapshots of the rest-mass density at $t_{\text{pb}} = 0.05, 1.40, 2.75,$ and 4.40 s for model M32-S075. The solid, dashed, and dotted curves denote surfaces with a density of $\rho = 10^{14} \text{ g cm}^{-3}$, with a neutrino optical depth of $\tau = 1$, and at the stalled shock, respectively. In the fourth panel, a BH is formed at the center (shaded region). In all the panels, the arrows display the poloidal velocity field (v^x, v^y). Their length is proportional logarithmically to the velocity. An animation of the rest-mass density for model M32-S075 is available in the online Journal. The 21 s animation runs from $t_{\text{pb}} = -0.68$ to 1.99 s.

(An animation of this figure is available.)

to $M_{\text{PNS}} = 2.0\text{--}2.5 M_{\odot}$ in $t_{\text{pb}} := t - t_{\text{b}} \sim 1$ s (see Figure 1). Here t_{b} denotes the time at the core bounce and we defined M_{PNS} to be the total rest mass in the region of $\rho \geq 10^{14} \text{ g cm}^{-3}$ (we note that due to this definition, a part of the rest mass of the dense region of the torus is included in M_{PNS} just prior to BH formation). Subsequently, M_{PNS} exceeds $3 M_{\odot}$ for all the rapidly rotating models listed in Table 1. This mass exceeds the maximum rest mass of the non-rotating cold NSs, which is $\approx 2.42 M_{\odot}$ and $\approx 2.89 M_{\odot}$ for the SFHo and DD2 EOSs, respectively. Thus, the centrifugal force (and partly the thermal pressure) plays a key role in preventing the collapse of the PNS to a BH for seconds. Along the rotation axis the rotational period becomes ~ 0.5 ms in the late stage of the PNS.

Together with the PNS, a massive torus is formed around it. Here, we define the torus mass by $M_{\text{torus}} := M_{\tau > 1} - M_{\text{PNS}}$, where $M_{\tau > 1}$ is the total rest mass in a region with an average optical depth of electron neutrinos and antineutrinos ($\tau \equiv (\tau_{\nu_e} + \tau_{\bar{\nu}_e})/2$) larger than unity. We find that the torus mass increases by matter infall and eventually far exceeds $1 M_{\odot}$. For the $M_{\text{He}} = 32 M_{\odot}$ models, this mass becomes very large in a short post-bounce time. The torus initially has a radius of ~ 200 km in the equatorial plane (see the second panel of Figure 2 for M32-S075; the dashed curve). During the growth of the torus, a standing accretion shock with a donut shape is formed surrounding the PNS and torus (the second panel of Figure 2; the dotted curve), and this shock expands gradually with time due to shock heating induced by the matter infall. Because of our choice of the initial angular-velocity profile, the matter that accretes onto the PNS and torus at late times has a smaller specific angular momentum. Because of its high mass and less specific centrifugal force at late times, the torus shrinks (its density increases; the third panel of Figure 2), and as a result, the value of M_{PNS} steeply increases prior to the formation of the BH (see the upper panel of Figure 1). For the larger value of R_0 for which the specific angular momentum of the matter in the outer region is larger, the mass accretion timescale is longer.

Shrinkage of the torus enhances the neutrino luminosity (see Figure 3 for the increase of it in late stages), in particular from the torus. The maximum neutrino luminosity is higher for higher values of M_{He} and could be close to $10^{54} \text{ erg s}^{-1}$, as found by Sekiguchi & Shibata (2011). Because the ram pressure produced by the infalling matter decreases with time, such a huge neutrino heating naturally leads to shock revival. The explosion occurs in particular toward the polar direction

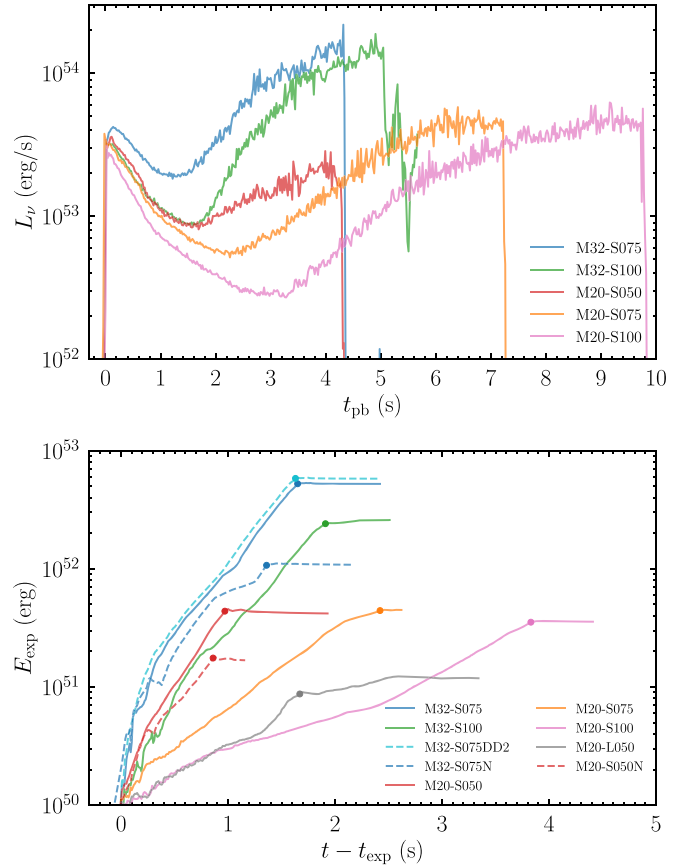


Figure 3. Top: Total neutrino luminosity as a function of post-bounce time. Bottom: Diagnostic explosion energy as a function of $t - t_{\text{exp}}$, where t_{exp} is the explosion time defined as the time at which the explosion energy exceeds 10^{50} erg. The filled circle on each curve denotes the BH formation time for each model.

for which the matter density and associated ram pressure are relatively small (see Figure 4). The explosion occurs qualitatively in the same manner for all the rapidly rotating models listed in Table 1.

Table 1 lists the diagnostic explosion energy, E_{exp} . Here, this explosion energy is evaluated in the computational region of $\lesssim 30,000$ km by integrating the positive binding energy of

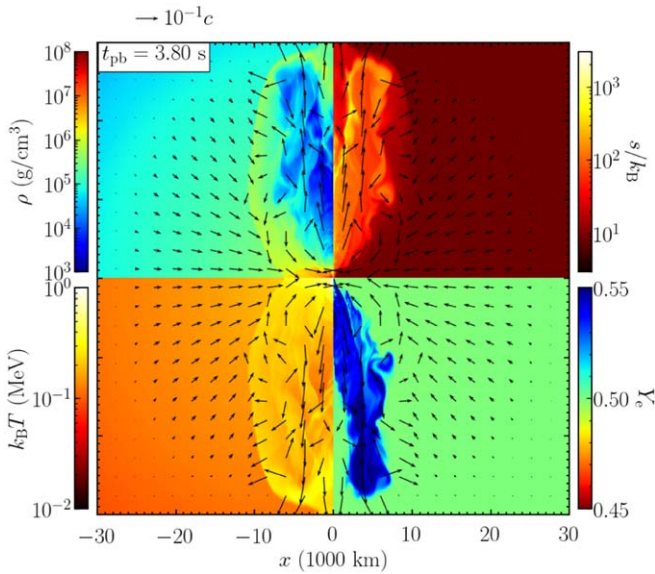


Figure 4. Snapshots of the rest-mass density (top-left), entropy per baryon (top-right), temperature (bottom-left), and electron fraction (bottom-right) at $t_{\text{pb}} = 3.80$ s for model M32-S075. k_B denotes Boltzmann’s constant. The arrows display the poloidal velocity field (v^x , v^y). Their length is proportional logarithmically to the velocity. An animation of this figure is available in the online Journal. The 7 s animation runs from $t_{\text{pb}} = 2.82$ to 4.47 s.

(An animation of this figure is available.)

the matter as done by Müller et al. (2012) (see Appendix A for our formulation of it). For the present explosion models, E_{exp} eventually exceeds 10^{51} erg, and for the $M_{\text{He}} = 32 M_{\odot}$ models, it becomes higher than 10^{52} erg, i.e., appreciably higher than the kinetic energy of typical SNe. This is a reflection of the neutrino luminosity by one order of magnitude higher than in for typical SNe (on the relation between the neutrino luminosity and explosion energy, see, e.g., Yamamoto et al. 2013). The explosion energy for models without the neutrino–antineutrino pair-annihilation process (M20-S050N and M32-S075N) is 2.5–4 times smaller than that for corresponding models with the process (see Table 1). This indicates that the pair-annihilation of neutrinos is the dominant process of the energy injection.

This larger neutrino-driven energy injection could be a substantial fraction of the energy injected for broad-line type-Ic SNe with a bipolar outflow (Maeda et al. 2002; Maeda & Nomoto 2003; Mazzali et al. 2005; Maeda et al. 2008). We note that the energy deposition rate to the outflow is $\gtrsim 10^{52}$ erg s^{-1} for the $M_{\text{He}} = 32 M_{\odot}$ models. Thus, ^{56}Ni with masses of 10^{-2} – $10^{-1} M_{\odot}$ may be synthesized in the ejecta (Tominaga et al. 2007, S. Wanajo et al. 2021 in preparation).

For model M32-S075DD2, the explosion energy is slightly higher than that for M32-S075, but the difference is not significant. This is because the lifetime of the PNS and the duration of the energy injection through neutrino heating are only slightly different between the two models with different EOSs due to the rapid increase of M_{PNS} to the critical mass for the gravitational collapse to a BH.

For the larger value of R_0 , the explosion is delayed and the explosion energy is smaller (e.g., compare the results of M20-S050 and M20-L050). The reason for this is that for the larger value of R_0 (for a given value of Ω_0), the increase of the torus mass is delayed due to the larger centrifugal force, and the specific neutrino emissivity is decreased at the late time at

which the explosion is driven (i.e., the formation timescale of the torus is as long as or longer than the neutrino-cooling one). This suggests that angular momentum distribution is key for controlling the explosion energy.

We also note that for model M32-S100, the massive torus remains, maintaining a high neutrino luminosity ($\gtrsim 10^{52}$ erg s^{-1}), after BH formation (see Figures 1 and 3). As a result, the neutrino-driven outflow is still present after BH formation. However, the neutrino luminosity is not enhanced significantly and the explosion energy is relatively low for this model, in spite of the formation of a massive torus. The reason for this is, again, that the formation timescale of the torus is as long as or longer than its neutrino-cooling one in this model. Hence, to enhance the neutrino luminosity far beyond 10^{53} erg s^{-1} , the torus has to form before sufficient neutrino cooling occurs. For achieving such a physical state, a pre-collapse progenitor with a compact core, which has angular momentum sufficiently large in its inner region with a steep cut-off at a radius, is likely to be necessary.

For the high-mass progenitors employed in this work, a BH is eventually formed due to continuous matter accretion onto the PNS, in particular from the equatorial direction. Since the central object gains a large amount of angular momentum from the rotating progenitor, the BH at formation is rapidly spinning with a dimensionless spin $\gtrsim 0.9$ irrespective of the models. The rest-mass density in the vicinity of the rotation axis becomes as low as $\lesssim 10^3$ g cm^{-3} after BH formation (see the fourth panel of Figure 2). The eventual total rest mass in the funnel region of $R \leq 50$ km and $|z| \leq 10^4$ km is $\lesssim 10^{-7} M_{\odot}$.

4. Summary and Discussion

This article proposes a new mechanism for driving energetic SNe like broad-line type-Ic SNe by neutrino heating. The model supposes that the progenitor stars of the SNe have sufficient high mass and rapid rotation to form a rapidly rotating PNS surrounded by a high-mass torus. The resulting PNS can survive for seconds due to strong centrifugal-force support, and in addition, due to the presence of a high-mass torus surrounding it, the total neutrino luminosity can be quite high at several seconds after core bounce. Then, the neutrino heating drives a high-energy SN, in particular toward the polar direction. In the successful explosion, the total rest mass of the central object becomes high enough (i.e., $\gtrsim 3 M_{\odot}$) and the explosion is significantly delayed, typically for seconds, after the core bounce (thus to study this model, we need a long-term general-relativistic simulation, only by which the criteria for the formation of the BH are accurately taken into account). In this case, the explosion occurs in a bipolar manner via neutrino heating. The explosion energy is beyond the typical explosion energy of SNe $\sim 10^{51}$ erg s^{-1} , and even larger than 10^{52} erg for high-mass progenitor models. Thus, this mechanism could provide (at least a part of) the energy injection needed for energetic SNe like broad-line type-Ic SNe.

Furthermore, a rapidly spinning BH is eventually formed. Since the polar outflow found in this paper produces a low-density funnel along the rotation axis, the remnant looks suitable for launching an ultra-relativistic jet, i.e., a GRB (Woosley 1993; MacFadyen et al. 2001; Woosley & Bloom 2006; Cano et al. 2017), in the presence of energy injection. We here note that the mechanism for launching the ultra-relativistic jet is not necessarily the same as that for inducing the bipolar outflow; e.g., an MHD process may be the source for GRBs; see, e.g., Piran (2004). If the

formed BH is surrounded by a magnetized massive torus, such a system could drive a relativistic jet by subtracting the rotational kinetic energy of the BH (Blandford & Znajek 1977). The relativistic jet could not only drive a GRB but also provide additional energy injection for the SN explosion. Thus, this model provides a scenario for the association of broad-line type-Ic SNe and GRBs.

However, in the angular-velocity profiles chosen in this paper, the matter initially located in large radii have small angular momenta. Thus, except for M20-L050, the torus mass is not very large after BH formation, and hence, in the present models, it is unlikely to subsequently cause long-term energetic phenomena powered by the accretion of torus matter onto a BH. In contrast, if the matter in the outer region initially has larger specific angular momenta than that in the central region, which may be a reasonable assumption when considering more realistic stellar evolution, a massive accretion torus can be formed after BH formation. In such a case, further activity of the system is expected. Exploring this possibility could be interesting future work.

The above speculation suggests that the presence or absence of activity after the bipolar explosion may depend on the angular momentum distribution of the progenitor star, and this may explain a variety of the activity duration of the central engine and a variety of the high-energy events associated with broad-line type-Ic SNe (Woosley & Heger 2006; Margutti et al. 2014; Lazzati et al. 2012) (see also Nakar 2015 on the importance of the density profile of the pre-collapse progenitor). Our numerical results also match with the speculation that rapidly rotating massive stars are likely to be the progenitors of energetic type-Ic SNe and GRBs (Fryer & Heger 2005; Yoon & Langer 2005; Woosley & Heger 2006; Aguilera-Dena et al. 2018).

Recent radiation-MHD simulations (in non-relativistic gravity) by Obergaulinger & Aloy (2017, 2020, 2021) and Aloy & Obergaulinger (2021) have shown that in the presence of rapid rotation, a high-mass progenitor star can explode by a combination of neutrino heating, rotation, and magnetic-field effects. Our results are similar to theirs, but our work shows that an energetic explosion can occur purely by the neutrino heating effect even in the absence of magnetorotational effects for the progenitor stars more massive than those employed by Obergaulinger & Aloy (2017, 2020, 2021), Aloy & Obergaulinger (2021). The only required condition for our case is the presence of sufficiently rapid rotation inside the stellar core.

In this paper, we present only models that produced an explosion. For low angular-momentum models, the PNS collapses to a BH before the explosion. Thus, to produce an explosion, the progenitor star needs to have sufficient angular momentum. Details on non-explosion models and approximate criteria for a successful explosion should be systematically studied.

There are several issues that need to be addressed to quantitatively improve the present work. First, our treatment of neutrino-radiation transfer is currently based on a gray leakage scheme. Obviously, simulations with a better radiation transfer code are needed.

The present work is based on axisymmetric simulations. Because the torus is massive, non-axisymmetric deformation is likely to take place in reality (e.g., Shibata & Sekiguchi 2005; Shibagaki et al. 2020). This may cause angular momentum transport in the torus and accretion onto the PNS may be

enhanced leading to earlier collapse to a BH. The angular momentum transport can also be enhanced by MHD effects, such as a magnetorotational instability (Mösta et al. 2014) and magnetic braking. Alternatively, MHD effects may help produce an earlier explosion if the magnetic field is amplified significantly by MHD instabilities (Obergaulinger & Aloy 2020, 2021). All these possibilities suggest that we need more sophisticated simulations. Thus, we plan to investigate MHD effects using a radiation-MHD code recently developed (Shibata et al. 2021a).

The non-axisymmetric deformation of the massive torus could also lead to the burst emission of gravitational waves. Our latest study shows that if a one-armed spiral deformation mode grows in a dynamical timescale comparable to the typical rotational period of the torus, the degree of the non-axisymmetric density fluctuation can be 10%–20% the torus mass (Shibata et al. 2021b). In such deformation, the maximum amplitude of burst-type gravitational waves at a hypothetical distance to the source of 100 Mpc can be $\sim 10^{-22}$ with a typical frequency of 0.7–0.8 kHz for $M_{\text{PNS}} \approx 3 M_{\odot}$ with a comparable torus mass (Shibata et al. 2021b). Such gravitational waves are interesting sources for third-generation gravitational-wave detectors such as the Einstein Telescope (Punturo et al. 2010) and Cosmic Explorer (Abbott et al. 2017). Thus, in the future, high-energy SNe with a bipolar outflow may be explored not only by electromagnetic telescopes but also by gravitational-wave detectors.

We thank T. Kuroda, K. Maeda, N. Tominaga, and S. Wanajo for useful discussions. This work was in part supported by Grant-in-Aid for Scientific Research (Grant Nos. JP20H00158) of Japanese MEXT/JSPS. Numerical computations were performed on Sakura and Cobra at Max Planck Computing and Data Facility and XC50 at National Astronomical Observatory of Japan.

Appendix A Diagnosis of the Explosion Energy

In this Appendix, we describe how to estimate the explosion energy in this work. The explosion energy is estimated for matter which are gravitationally unbound and located at a region far from the central object. In such a far region, the spacetime is approximately stationary and we may consider that an approximately time-like Killing vector exists. If $(\partial_t)^\mu$ is assumed to be the time-like Killing vector, the conservation equation of the energy density is described by:

$$\nabla_\mu T_t^\mu = \frac{1}{\sqrt{-g}} \partial_\mu (\sqrt{-g} T_t^\mu) = 0, \quad (\text{A1})$$

where $T_{\mu\nu}$ is the energy-momentum tensor of the matter, g is the determinant of the spacetime metric $g_{\mu\nu}$, and ∇_μ is the covariant derivative with respect to $g_{\mu\nu}$. Then, the conserved energy density and associated flux density, respectively, are defined by:

$$\begin{aligned} -\sqrt{-g} T_t^t &= -\alpha \sqrt{\gamma} (\rho h u_t u^t + P) \\ &= \alpha \sqrt{\gamma} (\rho h w^2 - P - \rho h u^t u_k \beta^k) \\ &= \rho_* (\alpha \hat{e} - \hat{u}_k \beta^k), \end{aligned} \quad (\text{A2})$$

$$\begin{aligned}
-\sqrt{-g}T_t^i &= -\alpha\sqrt{\gamma}\rho hu_i u^i = \alpha\sqrt{\gamma}(\rho hw^2 v^i - \rho hu^i u_k \beta^k) \\
&= \rho_* v^i (\alpha hw - \hat{u}_k \beta^k),
\end{aligned}
\tag{A3}$$

where $\rho_* = \rho w \sqrt{\gamma}$, $\hat{e} = hw - P/\rho w$, and $\hat{u}_i = hu_i$, which contain the lapse function α , the determinant of the spatial metric $\gamma(=-g/\alpha^2)$, the pressure P , specific enthalpy h , and $w = \alpha u^t$. The specific binding energy e_{bind} is then defined by:

$$\begin{aligned}
e_{\text{bind}} &= \frac{-\sqrt{-g}T_t^t}{\sqrt{-g}\rho u^t} - (1 + \varepsilon_{\text{min}}) \\
&= \alpha \hat{e} - \hat{u}_k \beta^k - (1 + \varepsilon_{\text{min}}).
\end{aligned}
\tag{A4}$$

Here, $\varepsilon_{\text{min}} \approx -0.0013$ is the minimum specific internal energy (including nuclear binding energy) in the employed EOS table. Note that this definition is slightly different from that of Müller et al. (2012) due to the presence of the shift vector $\hat{u}_k \beta^k$.

We define the explosion energy as the volume integral of the positive binding energy density of the matter, i.e., as:

$$\begin{aligned}
E_{\text{exp}} &= \int_{e_{\text{bind}}>0} d^3x \sqrt{-g} (T_t^t - \rho u^t (1 + \varepsilon_{\text{min}})) \\
&= \int_{e_{\text{bind}}>0, r < r_{\text{ext}}} d^3x \sqrt{-g} T_t^t \\
&\quad + \int dt \int_{e_{\text{bind}}>0, r=r_{\text{ext}}} ds_k \sqrt{-g} T_t^k - (1 + \varepsilon_{\text{min}}) M_{\text{ej}},
\end{aligned}
\tag{A5}$$

where ds_k is the area element of a sphere with radius r_{ext} , and M_{ej} is the ejecta mass defined by:

$$\begin{aligned}
M_{\text{ej}} &= \int_{e_{\text{bind}}>0} d^3x \sqrt{-g} \rho u^t = \int_{e_{\text{bind}}>0, r < r_{\text{ext}}} d^3x \rho_* \\
&\quad + \int dt \int_{e_{\text{bind}}>0, r=r_{\text{ext}}} ds_k \rho_* v^k.
\end{aligned}
\tag{A6}$$

Figure 5 compares the explosion energy defined in this Appendix with those produced by the methods of Müller et al. (2012) and Fujibayashi et al. (2020a) for models M32-S075 and M20-L050, which have the largest and smallest values of the explosion energy among the models with the SFHo EOS employed, respectively. Here, in Fujibayashi et al. (2020a), the ejecta was defined as the matter with $hu_t + h_{\text{min}} < 0$ based on Bernoulli's argument ($h_{\text{min}} \approx 1 + \varepsilon_{\text{min}}$ is the minimum specific enthalpy in the employed EOS table), and the explosion energy is calculated by:

$$\begin{aligned}
&\int_{hu_t + h_{\text{min}} < 0} d^3x \rho_* \left(\hat{e} - \frac{M}{r} - h_{\text{min}} \right) \\
&= \int_{hu_t + h_{\text{min}} < 0, r < r_{\text{ext}}} d^3x \rho_* \left(\hat{e} - \frac{M}{r} - h_{\text{min}} \right) \\
&\quad + \int dt \int_{hu_t + h_{\text{min}} < 0, r=r_{\text{ext}}} ds_k \rho_* v^k \left(\hat{e} - \frac{M}{r_{\text{ext}}} - h_{\text{min}} \right),
\end{aligned}
\tag{A7}$$

where the contribution of the gravitational binding energy is considered by adding $-GM\rho_*/r$ to the total energy density of the ejecta with the gravitational mass of the central object M , which is approximated by the enclosed baryon mass at the extraction radius in this case. Note that, of course, the criteria

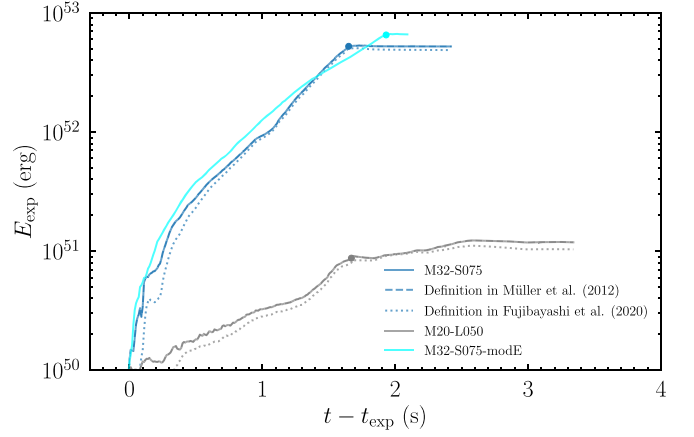


Figure 5. Diagnostic explosion energy as a function of $t - t_{\text{exp}}$ for models M32-S075 and M32-S075-modE. For model M32-S075, the explosion energy defined by Equation (A5) (solid), by Müller et al. (2012) (dashed), and by Equation (A7) (dotted) are shown.

used in Equations (A5) and (A7) have the same Newtonian (non-relativistic and weak-gravity) limit.

We find that the methods of estimating the explosion energy in Equation (A5) and by Müller et al. (2012) give very similar values. This implies that the contribution of the term with the shift vector ($\hat{u}_k \beta^k$) is negligible in this case. We also find that the values of the explosion energy defined by Equations (A5) and (A7) are different only slightly ($\approx 8\%$) for M32-S075. This is because at the extraction radius ($\approx 3 \times 10^4$ km), the flow is approximately stationary and Bernoulli's argument gives a good criterion for the ejecta. In addition, the contribution of the gravitational binding energy at the large radius is only $GM/c^2 r_{\text{ext}} \approx 0.05(M/10 M_{\odot})\%$ of the rest-mass energy, so that it is minor compared to the kinetic energy of the ejecta, and thus, the explosion energy does not depend strongly on the methods of its diagnosis. For model M20-L050, on the other hand, the difference of the explosion energy is relatively large, $\approx 16\%$, likely because the explosion is less energetic and the contribution of the gravitational binding energy is relatively large.

Appendix B

Effects of the Estimated Neutrino Energy Distribution

For the calculation of neutrino reaction rates, the energy distribution of (streaming) neutrinos needs to be assumed in our energy-integrated radiation-transfer scheme. Here, we illustrate the quantitative dependence of the explosion energy on the following assumptions.

In this work, we assume the Fermi–Dirac-type energy distribution of neutrinos in the form of:

$$f_{\nu}(\omega) = \frac{1}{e^{\omega/T_{\nu} - \eta_{\nu}} + 1},
\tag{B1}$$

where T_{ν} and η_{ν} are parameters to be determined. For determining them, we use the expression of the energy density of the streaming neutrinos in the comoving frame of the matter:

$$\begin{aligned}
J &= \int \frac{d^3k}{(2\pi\hbar)^3} \omega f_{\nu}(\omega) \\
&= \frac{T_{\nu}^4}{2\pi^2(\hbar c)^3} F_3(\eta_{\nu}),
\end{aligned}
\tag{B2}$$

where $F_i(\eta)$ is the relativistic Fermi integral of order i . We further assume $T_\nu = T$, i.e., the “temperature” of streaming neutrinos is assumed to be equal to the local matter temperature. In our simulation, the absorption and pair-annihilation of neutrinos are calculated using the energy distribution estimated above. Because the temperature of neutrinos in reality is comparable to the matter temperature in their emission region, which is usually higher than that in their free-streaming region, the assumption of $T_\nu = T$ is likely to introduce an underestimation of the neutrino heating rate to matter (i.e., in the present work, the neutrino heating is conservatively taken into account).

To quantitatively understand the magnitude of the underestimation, we perform a simulation with a different method to estimate the energy distribution as follows. Using the neutrino energy and number luminosity L_ν and $L_{N,\nu}$, we estimate the neutrino temperature as:

$$\frac{F_3(0)}{F_2(0)} T_\nu = \frac{L_\nu}{L_{N,\nu}}, \quad (\text{B3})$$

where we assumed $\eta_\nu = 0$, and defined:

$$L_\nu = \int d^3x \sqrt{-g} u_t Q_{(\text{leak})}, \quad (\text{B4})$$





$$L_{N,\nu} = \int d^3x \sqrt{-g} u_t \mathcal{R}_{(\text{leak})}. \quad (\text{B5})$$

Here, $Q_{(\text{leak})}$ and $\mathcal{R}_{(\text{leak})}$ are the energy and number emissivities in the rest frame of the matter, respectively (for details of their definition, see Sekiguchi 2010).

The simulation is performed using the same setup as M032-S075 (and the model is referred to as M032-S075-modE). In this model, the explosion occurs slightly earlier than in M32-S075, reflecting higher heating efficiency due to higher estimated neutrino average energy. Moreover, the explosion energy in this model is by $\approx 27\%$ higher than that for model M32-S075 (see Table 1). This indicates that with our fiducial energy-integrated method the explosion energy may be underestimated by 30%.

In reality, the systematic error may be even larger due to the following reason: the neutrino energy distribution estimated in both methods of this paper does not depend on the direction. However, the neutrino temperature should be larger for those emitted from the PNS than those from the torus, reflecting the difference of the matter temperature of the neutrino sphere, and this causes the angular dependence of the neutrino energy spectrum. To take into account such angular dependence of the energy distribution of neutrinos in the energy-integrated scheme, a more elaborated method (e.g., Foucart et al. 2016) is needed.

ORCID iDs

Sho Fujibayashi  <https://orcid.org/0000-0001-6467-4969>
 Koh Takahashi  <https://orcid.org/0000-0002-6705-6303>
 Yuichiro Sekiguchi  <https://orcid.org/0000-0002-2648-3835>
 Masaru Shibata  <https://orcid.org/0000-0002-4979-5671>

References

Abbott, B. P., Abbott, R., Abbott, T. D., et al. 2017, *CQGra*, 34, 044001
 Aguilera-Dena, D. R., Langer, N., Moriya, T. J., & Schootemeijer, A. 2018, *ApJ*, 858, 115

Alcubierre, M., Brüggmann, B., Holz, D., et al. 2001, *IJMPD*, 10, 273
 Aloy, M. Á., & Obergaulinger, M. 2021, *MNRAS*, 500, 4365
 Banik, S., Hempel, M., & Bandyopadhyay, D. 2014, *ApJS*, 214, 22
 Baumgarte, T. W., & Shapiro, S. L. 1999, *PhRvD*, 59, 024007
 Bethe, H. A., & Wilson, J. R. 1985, *ApJ*, 295, 14
 Blandford, R. D., & Znajek, R. L. 1977, *MNRAS*, 179, 433
 Bollig, R., Yadav, N., Kresse, D., et al. 2021, *ApJ*, 915, 28
 Burrows, A., Radice, D., & Vartanyan, D. 2019, *MNRAS*, 485, 3153
 Cano, Z., Wang, S.-Q., Dai, Z.-G., & Wu, X.-F. 2017, *AdAst*, 2017, 8929054
 Foucart, F., Duez, M. D., Hebert, F., et al. 2020, *ApJL*, 902, L27
 Foucart, F., O’Connor, E., Roberts, L., et al. 2016, *PhRvD*, 94, 123016
 Fryer, C. L., & Heger, A. 2005, *ApJ*, 623, 302
 Fujibayashi, S., Kiuchi, K., Nishimura, N., Sekiguchi, Y., & Shibata, M. 2018, *ApJ*, 860, 64
 Fujibayashi, S., Sekiguchi, Y., Kiuchi, K., & Shibata, M. 2017, *ApJ*, 846, 114
 Fujibayashi, S., Shibata, M., Wanajo, S., et al. 2020a, *PhRvD*, 101, 083029
 Fujibayashi, S., Wanajo, S., Kiuchi, K., et al. 2020b, *ApJ*, 901, 122
 Harada, A., Nagakura, H., Iwakami, W., et al. 2020, *ApJ*, 902, 150
 Hilditch, D., Bemuzzi, S., Thierfelder, M., et al. 2013, *PhRvD*, 88, 084057
 Janka, H. T. 2001, *A&A*, 368, 527
 Janka, H.-T., Hanke, F., Hüdepohl, L., et al. 2012, *PTEP*, 2012, 01A309
 Kuroda, T., Arcones, A., Takiwaki, T., & Kotake, K. 2020, *ApJ*, 896, 102
 Lazzati, D., Morsony, B. J., Blackwell, C. H., & Begelman, M. C. 2012, *ApJ*, 750, 68
 Liebendörfer, M., Mezzacappa, A., Messer, O. E. B., et al. 2003, *NuPhA*, 719, C144
 MacFadyen, A. I., & Woosley, S. E. 1999, *ApJ*, 524, 262
 MacFadyen, A. I., Woosley, S. E., & Heger, A. 2001, *ApJ*, 550, 410
 Maeda, K., Kawabata, K., Mazzali, P. A., et al. 2008, *Sci*, 319, 1220
 Maeda, K., Nakamura, T., Nomoto, K., et al. 2002, *ApJ*, 565, 405
 Maeda, K., & Nomoto, K. 2003, *ApJ*, 598, 1163
 Margutti, R., Milisavljevic, D., Soderberg, A. M., et al. 2014, *ApJ*, 797, 107
 Marronetti, P., Tichy, W., Brüggmann, B., González, J., & Sperhake, U. 2008, *PhRvD*, 77, 064010
 Mazzali, P. A., Kawabata, K. S., Maeda, K., et al. 2005, *Sci*, 308, 1284
 Mezzacappa, A., Marronetti, P., Landfield, R. E., et al. 2020, *PhRvD*, 102, 023027
 Mösta, P., Richers, S., Ott, C. D., et al. 2014, *ApJL*, 785, L29
 Müller, B. 2020, *LRCa*, 6, 3
 Müller, B., Janka, H.-T., & Marek, A. 2012, *ApJ*, 756, 84
 Nakamura, K., Takiwaki, T., & Kotake, K. 2019, *PASJ*, 71, 98
 Nakar, E. 2015, *ApJ*, 807, 172
 Obergaulinger, M., & Aloy, M. Á. 2017, *MNRAS*, 469, L43
 Obergaulinger, M., & Aloy, M. Á. 2020, *MNRAS*, 492, 4613
 Obergaulinger, M., & Aloy, M. Á. 2021, *MNRAS*, 503, 4942
 Piran, T. 2004, *RvMP*, 76, 1143
 Punturo, M., Abernathy, M., Acernese, F., et al. 2010, *CQGra*, 27, 194002
 Sekiguchi, Y. 2010, *PThPh*, 124, 331
 Sekiguchi, Y., & Shibata, M. 2011, *ApJ*, 737, 6
 Shibagaki, S., Kuroda, T., Kotake, K., & Takiwaki, T. 2020, *MNRAS*, 493, L138
 Shibata, M. 2000, *PThPh*, 104, 325
 Shibata, M., Fujibayashi, S., & Sekiguchi, Y. 2021a, *PhRvD*, 103, 043022
 Shibata, M., Kiuchi, K., Fujibayashi, S., & Sekiguchi, Y. 2021b, *PhRvD*, 103, 063037
 Shibata, M., Kiuchi, K., Sekiguchi, Y., & Suwa, Y. 2011, *PThPh*, 125, 1255
 Shibata, M., & Nakamura, T. 1995, *PhRvD*, 52, 5428
 Shibata, M., & Sekiguchi, Y.-I. 2005, *PhRvD*, 71, 024014
 Steiner, A. W., Hempel, M., & Fischer, T. 2013, *ApJ*, 774, 17
 Stockinger, G., Janka, H. T., Kresse, D., et al. 2020, *MNRAS*, 496, 2039
 Sumiyoshi, K., Fujibayashi, S., Sekiguchi, Y., & Shibata, M. 2021, *ApJ*, 907, 92
 Takahashi, K., Yoshida, T., & Umeda, H. 2018, *ApJ*, 857, 111
 Tominaga, N., Maeda, K., Umeda, H., et al. 2007, *ApJL*, 657, L77
 Woosley, S. E. 1993, *ApJ*, 405, 273
 Woosley, S. E., & Bloom, J. S. 2006, *ARA&A*, 44, 507
 Woosley, S. E., & Heger, A. 2006, *ApJ*, 637, 914
 Woosley, S. E., Heger, A., & Weaver, T. A. 2002, *RvMP*, 74, 1015
 Yamamoto, Y., Fujimoto, S.-i., Nagakura, H., & Yamada, S. 2013, *ApJ*, 771, 27
 Yoon, S. C., & Langer, N. 2005, *A&A*, 443, 643